Evidence of midmantle anisotropy from shear wave splitting and the influence of shear-coupled *P* waves

J. Wookey and J.-M. Kendall
School of Earth Sciences, University of Leeds, Leeds, UK

Received 30 October 2003; revised 29 April 2004; accepted 18 May 2004; published 23 July 2004.

[1] Until recently, the midmantle region of the Earth (the transition zone and the uppermost lower mantle) has been considered isotropic. Recent work by *Wookey et al.* [2002] presented evidence of anisotropy in the midmantle region near the Tonga-Kermadec subduction zone, inferred from shear wave splitting in teleseismic *S* phases at Australian seismic stations. This data set is revisited to examine the possibility of contamination by shear-coupled *P* waves. Using reflectivity modeling, we explore the effects of these phases on the measurement of shear wave splitting. Contamination of such measurements is demonstrated for short epicentral distances ($\Delta \sim 30°$). Wave field decomposition is a simple technique which can be used to separate these phases from the main *S* wave arrival. The Tonga-Australia data set is reprocessed after wave field decomposition. Shear wave splitting ranging between 0.7 and 6.2 s is observed, a range comparable to that observed by *Wookey et al.* [2002]. As before, the polarization of the fast shear wave is observed to be predominantly horizontal. However, the magnitudes of splitting for several events at short epicentral distances are significantly reduced, suggesting some influence of shear-coupled *P* waves in the original analysis. The results are compared with possible models of mantle anisotropy, and the results can be best explained by significant anisotropy in the midmantle region. The best candidate location for this anisotropy is in the uppermost lower mantle, and scenarios involving the alignment of lower mantle or subducted materials by regional dynamic processes are suggested to account for this. *INDEX TERMS:* 7203 Seismology: Body wave propagation; 8120 Tectonophysics: Dynamics of lithosphere and mantle—general; 9330 Information Related to Geographic Region: Australia; *KEYWORDS:* anisotropy, shear wave splitting, midmantle

Citation: Wookey, J., and J.-M. Kendall (2004), Evidence of midmantle anisotropy from shear wave splitting and the influence of shear-coupled *P* waves, *J. Geophys. Res.*, *109*, B07309, doi:10.1029/2003JB002871.

1. Introduction

[2] Seismic anisotropy, the variation of seismic wave velocity with direction, is an important tool in the understanding of the dynamics of deep Earth processes. Under favorable conditions it can provide a seismic signature to mantle flow invisible to other methods (such as tomography). Anisotropy has been extensively observed in the upper mantle (see reviews by *Silver* [1996], *Montagner* [1998], *Savage* [1999], and *Kendall* [2000]) and to a lesser extent the lowermost mantle (see reviews by *Lay et al.* [1998] and *Kendall and Silver* [1998]). Anisotropy in the mantle is most often associated with the lattice-preferred orientation (LPO) of anisotropic minerals or the shape-preferred orientation (SPO) of included materials such as melt. The LPO of olivine in the upper mantle has been attributed to many observations of anisotropy. This alignment is thought be to caused by present-day plate motions for oceanic lithosphere [e.g., *Babuška et al.*, 1998] and by more complex flow patterns at subduction zones [*Russo and Silver*, 1994; *Fischer et al.*, 1998; *Brisbourne et al.*, 1999] and mid-ocean ridges [*Blackman et al.*, 1993; *Wolfe and Solomon*, 1998]. The SPO alignment of inclusions has also been postulated as the cause of observations of anisotropy at mid-ocean ridges [*Kendall*, 1994; *Braun et al.*, 2000]. Anisotropy observed at the base of the mantle also has been associated both with the LPO of lower mantle minerals (perovskite, magnesiowüstite and stishovite) [e.g., *Karato*, 1998] and the SPO of aligned melt inclusions [e.g., *Thomas and Kendall*, 2002].

[3] Observations of anisotropy in the midmantle region (the transition zone and the upper part of the lower mantle) are much scarcer. Global studies using surface waves [*Trampert and Van Heijst*, 2002] and by reconciling body wave and normal mode reference models [*Montagner and Kennett*, 1996] suggest significant anisotropy at this level. In body wave studies, *Chen and Brudzinski* [2003] detected anisotropy in the transition zone beneath Tonga-Fiji attributed to a remnant of subducted slab. *Fouch and Fischer* [1996] report isolated regions of anisotropy in the upper transition zone (410–520 km) below the Kuril Islands, which they attribute to the preferential alignment of wadsleyite. Other studies have found no evidence for

0148-0227/04/2003JB002871$09.00

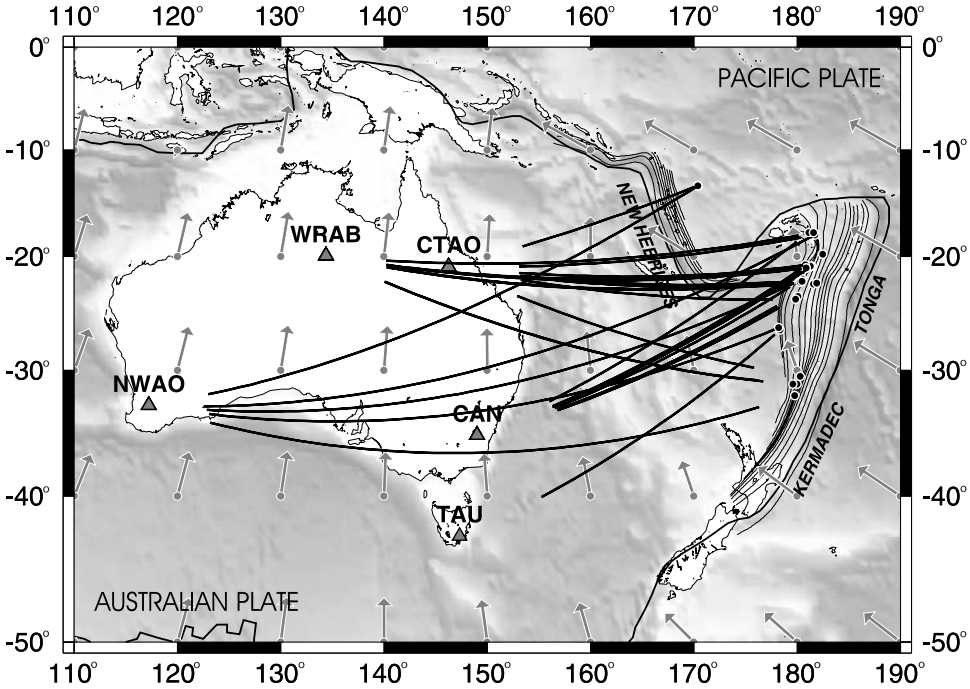

Figure 1. Map showing locations of events (circles), stations (triangles), and IASP91 [*Kennett and Engdahl*, 1991] predicted ray paths in the lower mantle. Also shown are plate motions in the hot spot reference frame (arrows) and plate boundaries [*Gripp and Gordon*, 1990], topography/bathymetry from *Smith and Sandwell* [1997], and depth of seismicity of the Tonga, Kermadec, and New Hebrides subduction zones from *Gudmundsson and Sambridge* [1998].

anisotropy in the midmantle [*Kaneshima and Silver*, 1992; *Fischer and Wiens*, 1996]. *Wookey et al.* [2002] (hereinafter referred to as WKB) report evidence of significant shear wave splitting in teleseismic direct *S* phases recorded at Australian continental stations from deep earthquakes in the Tonga, Kermadec, and New Hebrides trenches. They use modeling to infer a midmantle origin of this anisotropy. This work elicited a comment [*Saul and Vinnik*, 2003; *Wookey et al.*, 2003] suggesting that shear-coupled *P* waves may appear in the coda of the waveform and contaminate the shear wave splitting analysis, and hence the inference of midmantle anisotropy. In this study we examine the problems associated with the effect of shear-coupled *P* waves on teleseismic shear wave splitting analysis and apply a wave field decomposition technique as a solution. We reprocess the data set studied by WKB and assess the robustness of the conclusions.

1.1. Southwest Pacific Subduction

[4] Tectonic plate subduction is occurring in several places in the southwest Pacific. In the Tonga and Kermadec trenches the Pacific plate is being subducted westward beneath the Australian plate, and at the New Hebrides trench the Australian plate is being subducted northeast beneath the Pacific plate (see Figure 1). The rate of subduction is very high, exceeding 20 cm/yr in the Tonga trench [*Bevis et al.*, 1995]. Figure 1 also shows contours of the Wadati-Benioff (seismogenic) zone [*Gudmundsson and Sambridge*, 1998]. The morphology of subduction in these regions is complex. The New Hebrides slab appears to descend almost vertically, with a termination of seismicity near a depth of 400 km. There is, however, a cluster of very deep earthquakes near the 660 km discontinuity in the North Fiji basin. It has been suggested that these are not related to present-day subduction [*Hamburger and Isacks*, 1987]; however, tomography of the New Hebrides slab [*Widiyantoro et al.*, 1999; *Hall and Spakman*, 2002] shows a high-velocity anomaly extending to the 660 km discontinuity (and below) in the vicinity of these events. Beneath the Tonga trench the plunge of the slab is more shallow, and seismicity is observed all the way to the 660 km discontinuity. To the south, in the Kermadec trench, the subduction is again steeper to around 400 km and then appears to deflect to a shallower angle. The subduction zones (especially the Tonga slab) are very seismically active, providing a rich source of deep earthquakes.

1.2. Shear Wave Splitting Analysis

[5] The most common method of studying deep Earth anisotropy with body wave phases is the analysis of shear wave splitting. When a shear wave encounters an anisotropic medium, two orthogonal waveforms are generated, one propagating faster than the other. The two shear waves separate in time as they propagate. This delay and the polarization of the two waves persist after they have left the anisotropic medium and can be recorded at the surface. This also induces elliptical particle motion, often diagnostic of anisotropy. A commonly applied method for the analysis of shear wave splitting in body wave phases is the eigenvalue method of *Silver and Chan*

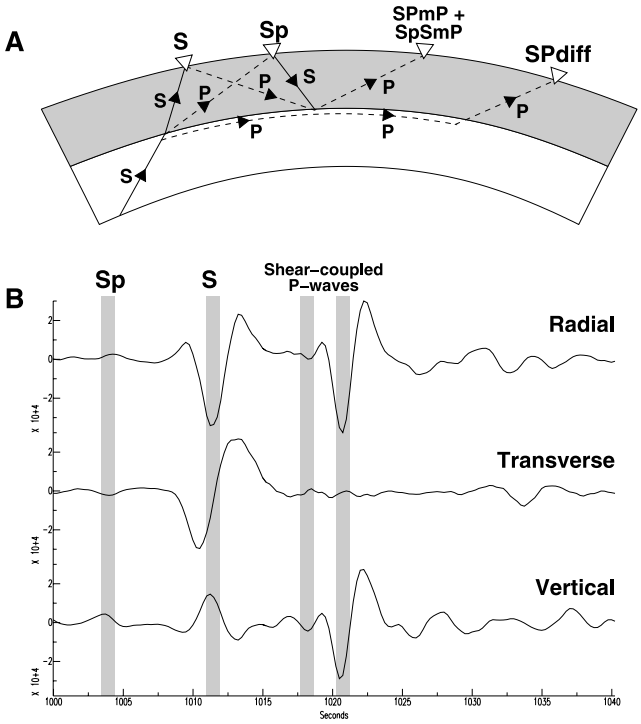

Figure 2. (a) Ray paths of shear-coupled *P* waves and (b) an event in which these phases are clearly observed. The event is an intermediate depth (85 km) earthquake in Peru, identified by *Zandt and Randall* [1985], recorded at station RSCP in western Tennessee (epicentral distance, $\Delta = 54.5°$). It shows two arrivals after *S*, identified as multiples from the Moho and a deeper discontinuity and a precursory *Sp* arrival.

[1991] (hereinafter referred to as SC). This method attempts to minimize the effect of anisotropy on a pair of horizontal seismograms by correcting for a range of possible lag times (δt) and fast directions (ϕ), implemented as a grid search. For each pair of values (each node on the grid) the eigenvalues of the covariance matrix of the two horizontal components are calculated. The best fitting δt and ϕ correspond to the point with smallest second eigenvalue. These parameters best linearize the ellipticity of the particle motion. The error in the results is estimated by applying a statistical *F* test and using the extent of the 95% confidence interval. This method is only applicable to shear waves which do not show complex particle motion in normal isotropic models. This is not the case for S_{diff} and *ScS* (at large epicentral distances), for example. The *S* wave phase itself begins to show elliptical particle motion outside the "shear wave window" [see, e.g., *Booth and Crampin*, 1985] at angles of incidence greater than 35°, due to the generation of postcritical evanescent waves.

1.3. Results Presented by *Wookey et al.* [2002] (WKB)

[6] WKB apply the SC shear wave splitting technique to direct *S* phases from deep (>350 km) earthquakes in the New Hebrides, Tonga, and Kermadec trenches recorded at stations on the Australian continent (see Figure 1 for event and station locations). From 164 initial measurements, WKB reduce the data set to the 35 measurements with the best estimated level of confidence. They report significant splitting in these phases with δt ranging from 0.7 to 7.1 s and a near-horizontal fast shear wave polarization (average 111°). On the basis of the magnitude of these results and the absences of splitting in the more vertical (angle of incidence 6–10° compared to 22–29°) *SKS*/*SKKS* phases at the Australian stations [*Clitheroe and van der Hilst*, 1998; *Barruol and Hoffmann*, 1999; *Özalaybey and Chen*, 1999], WKB infer a midmantle location for the anisotropy. They further use modeling to constrain the results and conclude that the most likely location for the anisotropy is beneath the 660 km discontinuity, in the locality of the subduction zone. Scenarios suggested for this anisotropy include (1) the alignment of lower mantle perovskite by flow associated with mantle convection or subduction or (2) the presence of an inclusion anisotropy involving subducted material. The problem highlighted by *Saul and Vinnik* [2003] with this analysis is that no account is taken for the possible degradation of the results by the presence of shear-coupled *P* waves in the coda of the *S* wave arrival. At the range of epicentral distances studied, the *S* wave is not as vertically incident at the surface as the *SKS*/*SKKS* phases to which shear wave splitting analysis is more normally applied. This nonvertical incidence means that generated reverberations may have a significant enough amplitude to interfere with *S* wave coda.

2. Shear-Coupled *P* Waves

2.1. Observations

[7] When a nonvertically traveling shear wave arrives at the free surface it generates downgoing reflections and conversions. These phases can be returned to the surface as further reflections and conversions from the Moho and deeper discontinuities in the Earth and appear in the coda of the primary *S* wave arrival. Figure 2a shows a schematic of the ray paths of these arrivals. *Zandt and Randall* [1985] observed these phases for teleseismic direct shear waves recorded in North America. Figure 2b shows one of the events reported. This is a teleseismic *S* wave from an intermediate depth earthquake (85 km) recorded at station RSCP in western Tennessee (an epicentral distance of 55°). This event shows a precursory *Sp* arrival (an *S*-to-*P* conversion at depth) and, more significantly, large arrivals some 10 s after the main *S* phase. These are interpreted as a weak *SPmP* arrival followed by a much stronger *SPhP* arrival (a reflection from an upper mantle discontinuity at around 75 km in depth beneath RSCP). Zandt and Randall note that the magnitudes of these phases are much larger than can be predicted by their waveform modeling and suggest that velocity gradients or layering might account for this discrepancy. Station RSCP shows well-constrained *SKS* splitting [*Silver and Chan*, 1991]. We therefore analyze the splitting in the teleseismic *S* wave for this event using the technique outlined above to assess the problem of shear-coupled *P* wave interference. Figure 3 shows this analysis. The analysis is performed twice; in the first case we window out the obvious shear-coupled *P* wave arrival, and in the second case we extend the window to include

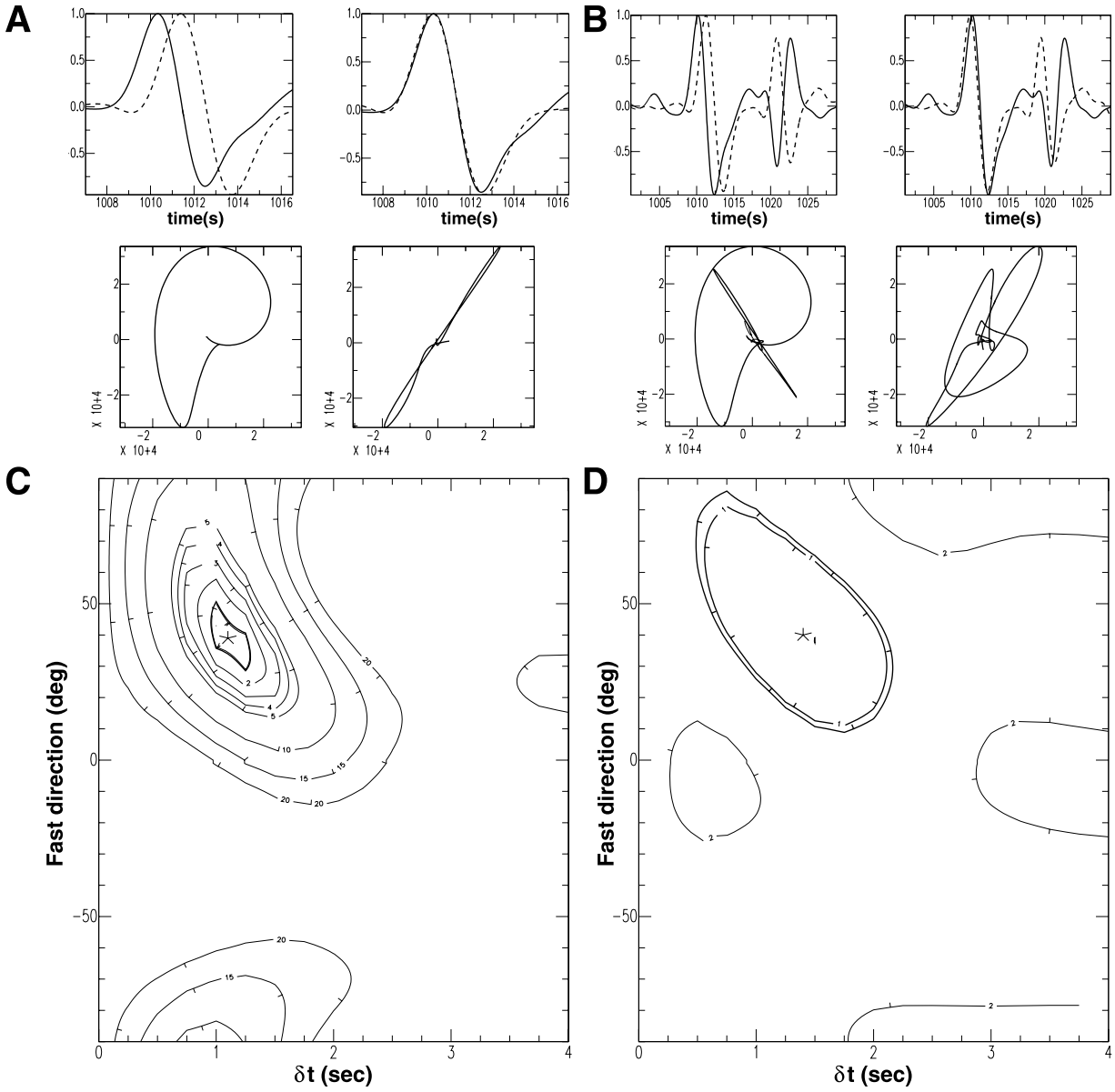

Figure 3. Splitting analysis of an event showing strong shear-coupled *P* waves identified by *Zandt and Randall* [1985]. This event is an intermediate depth (85 km) earthquake in Peru, recorded at station RSCP in western Tennessee (epicentral distance, $\Delta = 54.5°$). (a) and (c) Results of shear wave splitting analysis with the strong shear-coupled *P* wave arrival windowed out, and (b) and (d) results with the phase included. The results ($\delta t = 1.10 \pm 0.10$ s, $\phi = 41 \pm 4°$ for the small window, and $\delta t = 1.40 \pm 0.40$ s, $\phi = 40 \pm 20°$ for the longer window) show the same solution, but including the shear-coupled *P* wave arrivals reduces the level of confidence. The recovered fast direction is compatible with that determined for *SKS* ($59 \pm 6°$ [*Silver*, 1996]), but the lag time is greater (0.75 ± 0.15 s). This may be due to source-side anisotropy (event is in the olivine upper mantle) or the different incidence angle of the phase.

it. The first analysis gives a $\delta t = 1.10 \pm 0.10$ s and $\phi = 41 \pm 4°$, results which are similar to those observed for the *SKS*/*SKKS* phase by *Silver and Chan* [1991] ($\delta t = 0.75 \pm 0.15$ s and $\phi = 59 \pm 6°$). The difference between these may be due to a contribution from anisotropy in the source region. When the window is extended to include the shear-coupled *P* phase, the best fitting solution is unchanged, but the estimated error in the result increases significantly (from ± 0.15 s/$\pm 6°$ to ± 0.4 s/$\pm 20°$ in δt and ϕ, respectively). This is due to the fact that the contribution to λ_2 from the shear-coupled *P* wave is not minimized by the splitting correction. This suggests that significant shear-coupled *P* wave energy in the analysis window would significantly degrade the estimate of confidence in the shear wave splitting result.

2.2. Effects of *P* Wave Energy on Shear Wave Splitting

[8] The presence of *P* wave energy on the horizontal components of a seismogram could conceivably affect the shear wave splitting analysis by interfering with the

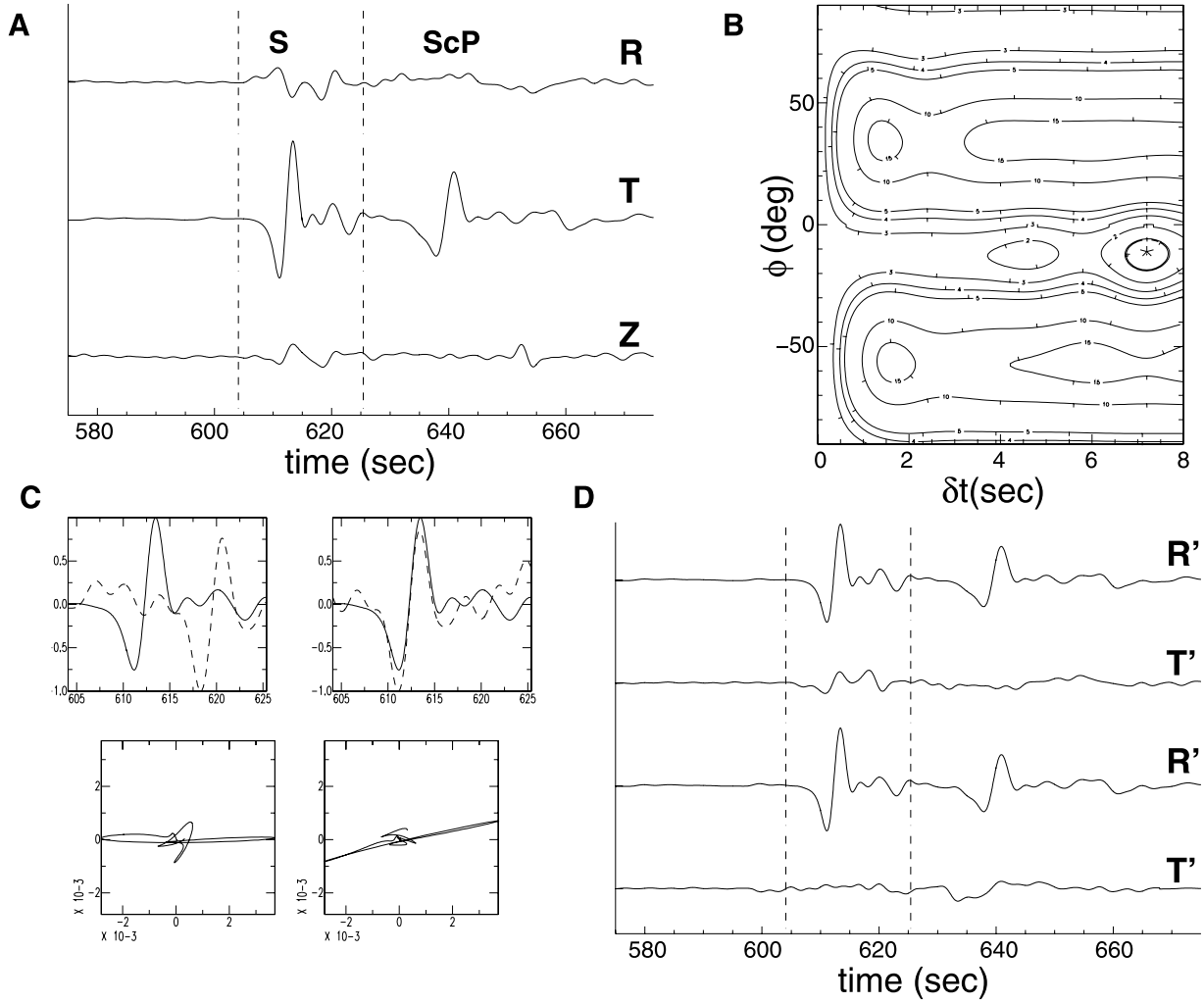

Figure 4. Shear wave splitting analysis of an isotropic reflectivity synthetic. (a) Radial, transverse and vertical components of the input seismogram. (b) Results of the grid search over δt and ϕ, with the best solution indicated by the star. (c) The (amplitude normalized) fast and slow *S* wave waveform comparison and particle motion before and after the anisotropy correction. (d) Horizontal components (top) before and (bottom) after the anisotropy correction, rotated into the inferred polarization direction of the initial (linear) shear wave pulse. Successful correction is indicated by removal of energy from the initial transverse component (T′). In this case, though the solution is well constrained, the particle motion before correction is already highly linear, suggesting that there is something amiss with this result. The measured shear wave splitting parameters are $\delta t = 7.20 \pm 0.25$ s and $\phi = -11 \pm 3°$.

S waveform (as noted by *Saul and Vinnik* [2003]). This interference might induce ellipticity in the particle motion and be misinterpreted as the effects of anisotropy. In order to test this possibility we use reflectivity modeling [*Mueller*, 1985] to generate four sets of synthetic three-component seismograms, each matching the event-station parameters (hypocenter depth, epicentral distance, approximate moment tensor) of an event from the data set of WKB. The distances considered are 24°, 32°, 42°, and 59°. The velocity model used is AK135, an isotropic, radially symmetric reference model [*Kennett et al.*, 1995]. Shear wave splitting analysis is then applied to these *S* waves. In three out of the four cases this gives null results (no constraint on the splitting solution), but for the model with a distance of 32° a falsely positive result is found. Figure 4 shows this example. In this case it appears that a portion of teleseismic *SP* phase (predicted to arrive around 6.5 s after the main *S* phase) on the radial component is "mistaken" for the slow shear wave. Despite the splitting algorithm assigning small errors to the recovered δt (splitting time) and ϕ (fast direction), there are indications that there is something amiss with this result. While there is a good match between the normalized fast and slow shear wave, the particle motion before correction is already highly linear (Figure 4c). This is relatively easy to diagnose in isotropic synthetic data, however in real data where noise is present this might not be so clear. If there is some anisotropy-induced splitting in the data, the analysis should properly identify the correct slow shear wave as this should give the smallest λ_2 (as in Figure 3). It also is evident from the input seismograms that there is shear wave energy on the

vertical component. Ideally, we would like to separate the P and S wave fields for our analysis.

3. Wave Field Decomposition

[9] In order to remedy the potential problems caused by nonvertical shear wave incidence at the free surface we need a method to both remove extraneous P wave energy from the radial components and to recover S wave energy from the vertical component. A simple and convenient way to do this is using wave field decomposition. This is similar to the method applied by *Tong et al.* [1994] to study the splitting in short distance S wave phases. *Kennett* [1991] presents a simple method of decomposing the P wave and S wave signal at the Earth's surface in three-component data for single stations (formulation presented is after *Bostock* [1998]).

[10] This method separates the contributions to a recorded surface displacement of the *P*, *SV*, and *SH* components of an arriving phase. In essence, it assumes a plane wave arrival of a known slowness (and hence incidence angle) and calculates the instantaneous projection of the recorded [*R*, *T*, *V*] displacement onto the directions corresponding to the [*P*, *SV*, *SH*] coordinate system.

[11] The ground displacement recorded at a seismogram can be expressed as

$$\mathbf{u}(0) = \mathbf{M}\mathbf{w}(0), \tag{1}$$

where $\mathbf{u} = [U_R, U_T, U_Z]'$ is the ground motion at the surface in the radial, transverse, and vertical directions. This is related to the upgoing *P*, *SV*, and *SH* wave field $\mathbf{w} = [P, SV, SH]'$ by the transition matrix $\mathbf{M}$. All quantities are expressed in the frequency-slowness (ω, p) domain. $\mathbf{M}$ is a 3×3 matrix, which for isotropic media, decouples into a 2×2 matrix describing *P-SV* motion and a scalar relation for *SH* motion. An estimate of $\mathbf{M}^{-1}$ is required in order to recover the upgoing wave field from the ground displacement. In isotropic media this can be expressed in a simple analytical form involving the P and S wave velocities, α and β, and the (horizontal) slowness, p, of the phase of interest,

$$\begin{pmatrix} P \\ S_V \\ S_H \end{pmatrix} = \begin{pmatrix} \dfrac{p\beta^2}{\alpha} & 0 & \dfrac{\beta^2 p^2 - \frac{1}{2}}{\alpha q_\alpha} \\ \dfrac{\frac{1}{2} - \beta^2 p^2}{\beta q_\beta} & 0 & p\beta \\ 0 & \frac{1}{2} & 0 \end{pmatrix} \begin{pmatrix} U_R \\ U_T \\ U_Z \end{pmatrix}, \tag{2}$$

where the vertical P wave slowness is $q_\alpha = \sqrt{\alpha^{-2} - p^2}$ and the vertical S wave slowness is $q_\beta = \sqrt{\beta^{-2} - p^2}$. These quantities are frequency-independent (see discussion by *Kennett* [1991]), so this operation can be carried out by straightforward matrix multiplication in the time domain, using the radial, transverse, and vertical traces as input and recovering the decomposed *P*, *SV*, and *SH* traces as output. The slownesses of the phases in our data are small enough to not exceed the critical angle of incidence; thus elliptical particle motion induced by evanescent waves should not be an issue [see, e.g., *Booth and Crampin*, 1985]. Since the quantities in $\mathbf{M}^{-1}$ vary gradually as a function of slowness, it is generally adequate for hard rock sites to use the reference model velocities [*Kennett*, 1991]. Also, although the slownesses of the primary S phase and subsequent P wave multiples are slightly different, they are close enough for the method to work satisfactorily. Since the slowness of the phase is not easily obtained from a single station, it is necessary to use that predicted by a reference model for the appropriate epicentral distance and depth. As will be demonstrated, this is adequate for our purposes.

4. Reprocessing the Tonga-Australia Shear Wave Splitting Data

[12] The crustal thickness beneath the stations used by WKB varies between 32 and 50 km, with all but one of the stations (TAU), having a Moho deeper than 40 km [*Clitheroe et al.*, 2000]. Figure 5 shows the relationship between epicentral distance and the arrival time after the main S phase of an *SPmP* Moho multiple for three values of crustal thickness and the teleseismic *SP* phase. We use ray tracing to calculate travel times for the IASP91 [*Kennett and Engdahl*, 1991] model, with a 500 km deep source. The onset of *SPmP* varies between 5.5 and 11.3 s for the range of epicentral distances and Moho depths in our data. For the far-offset events recorded at the continental stations, there should be sufficient separation such that any shear-coupled P wave energy falls outside the analysis window; however, the shorter-offset results might be affected. Interference from teleseismic *SP* (a reflecting free surface conversion) is also possible. This is the phase which seems to have caused the contamination of the synthetic result in Figure 4 and is predicted to appear across the whole range of epicentral distances in our data set, at delay times ranging between 5.7 and 14.4 s. Figure 6 shows the predicted difference between the slowness of the main S wave phase and *SPmP*, *SP*. Again, this was calculated using ray tracing assuming IASP91 reference model [*Kennett and Engdahl*, 1991] velocities. For the Moho multiple phases the difference is very small (less than 0.15 s/deg). The *SP* phase shows a small difference until $\Delta = 50°$, then it begins to increase rapidly. This is also where the delay of the phase begins to increase. From this we conclude that the wave field decomposition should also be effective at separating it from the shear wave where it is likely to contaminate the S phase arrival. The *SPmP* phase should be separable over the whole range of epicentral distances. For multiple arrivals from deeper interfaces (such as that identified by *Zandt and Randall* [1985], where the slowness difference will be larger) the longer delay time (and weaker amplitude) should prevent it interfering with the analysis. An example of the effectiveness of this is shown in Figure 7. This is the grid search results for the synthetic example shown in Figure 4b, after the wave field decomposition has been applied to the data. The apparently well-constrained false solution shown in Figure 4b has been degraded to a level where it is unbounded by the 95% confidence interval; thus the inferred errors are

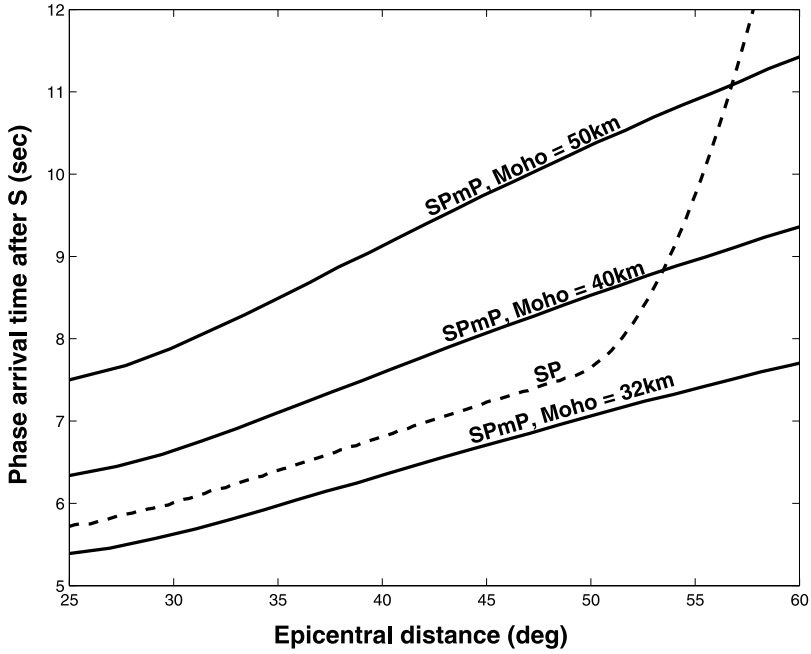

Figure 5. Delay time after *S* of a shear-coupled *P* wave multiple from the Moho at depths of 32, 40, and 50 km (solid lines) and the *SP* phase (dashed line) as a function of epicentral distance. This was calculated using crustal velocities and slownesses from the IASP91 reference model [*Kennett and Engdahl*, 1991] for a 500 km deep source.

very much larger (in δt from ±0.25 to ±7.35 and in ϕ from ±3° to ±23°). This would naturally lead to the rejection of the result.

[13] In order to examine the possibility of contamination of the results presented by WKB by *P* wave energy on the horizontal components we reprocess the Tonga-Australia data set using the wave field decomposition technique prior to shear wave splitting analysis.

4.1. Results

[14] An example of the effect of the wave field decomposition on the shear wave splitting analysis is

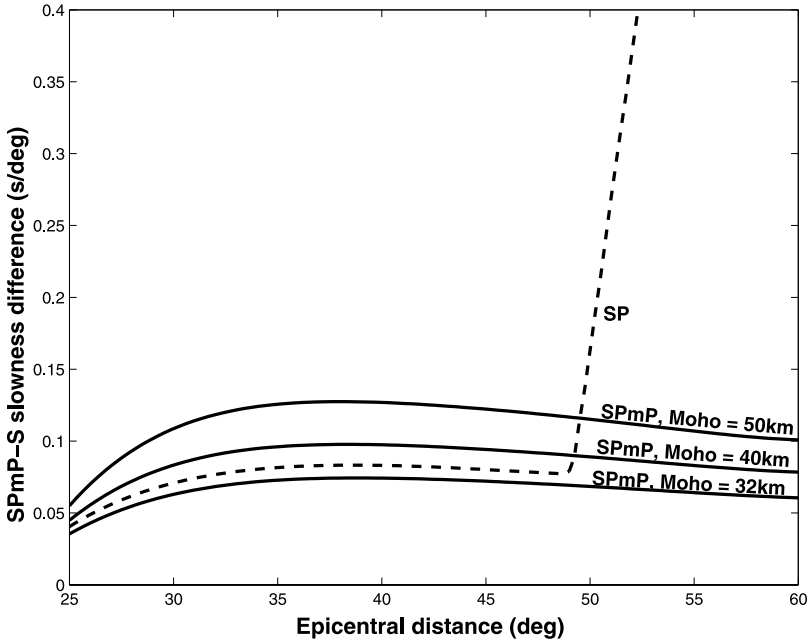

Figure 6. Difference in slowness between main *S* phase and a shear-coupled *P* wave multiple from the Moho at depths of 32, 40, and 50 km (solid lines) as a function of epicentral distance. The *SP* is also shown (dashed line). This was calculated using crustal velocities and slownesses from the IASP91 reference model [*Kennett and Engdahl*, 1991] for a 500 km deep source.

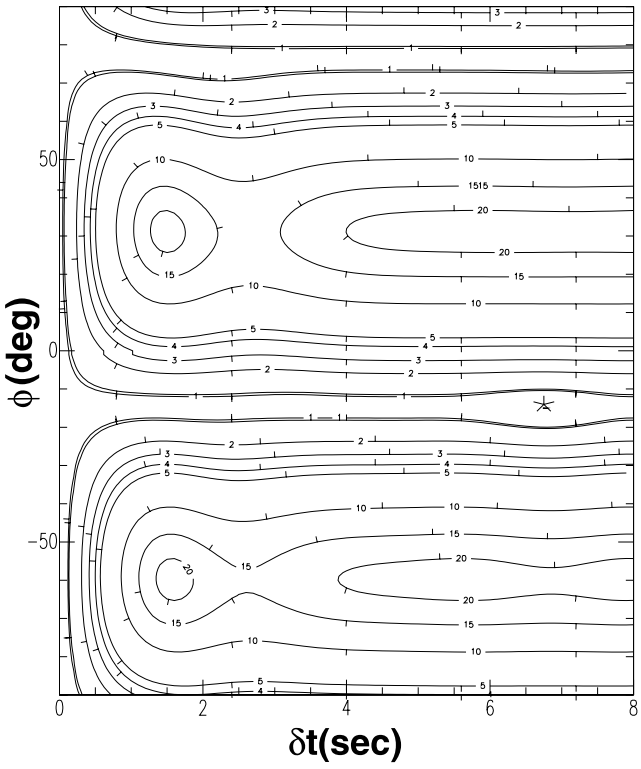

Figure 7. Shear wave splitting analysis of the isotropic reflectivity synthetic in Figure 4 after wave field decomposition. The false confidence in the solution shown in Figure 4b has been removed, and the solution returned by this analysis has large errors ($\delta t = 6.75 \pm 7.35$ s and $\phi = -14 \pm 23°$) as it is unbounded by the 95% confidence interval.

shown in Figure 8. It is clear that the postdecomposition seismograms give a much improved measurement. The errors on δt and ϕ are smaller, and the resulting minimization of transverse energy, particle motion plots, and constraint in the solution are all more convincing. It appears, however, in this example that the improvement may be less related to interference from *P* wave phases (the *P* wave component in the analysis window is fairly quiet) and more due to the recovery of shear wave energy from the vertical component. The recovered δt is somewhat smaller, though the new result does fall within the error bounds of the old. The waveforms studied are, in general, more complex than those associated with the analysis of shear wave splitting in *SKS* phases because of the influence of heterogeneity in the source region and receiver effects. Where this complication degrades the shear waveforms, however, we expect a poor solution from shear wave splitting analysis. This highlights the importance of reducing the data set to the best results only. We also do not see elliptical particle motion in all cases, even for the best results. This simply occurs when the splitting time δt approaches the dominant period of the phase. The eigenvalue method of *Silver and Chan* [1991] is still valid for this case.

[15] Figure 9 shows further examples of measurements of splitting from the reprocessed Tonga-Australia data set. Since these events have smaller splitting times (δt = 1.5–2.2 s), they show the elliptical particle motion more generally associated with shear wave splitting. The splitting correction for these events is also rather convincing, producing in all cases strongly linear particle motion and a good waveform match. All of these events show more splitting than can be explained by even an optimistic estimate of anisotropy in the upper mantle below the stations (see Figure 10b).

[16] In Figure 10a we show the data from WKB and the reprocessed results plotted as a function of epicentral distance. The wave field decomposition clearly does have some impact on the shear wave splitting results. Several of the large splits identified in WKB now give smaller values than before, and the average value is reduced; for the original data the average δt is 2.58 ± 0.2 s and with the decomposition it is 1.89 ± 0.2 s. Despite this, there are still large splitting values, including one result with δt = 6.2 ± 0.3 s. The analysis for this result is shown in Figure 11. Figure 11 shows a negligible amount of energy on the *P* wave component and clear splitting which is corrected by the process. It should be noted that the lack of initial elliptical particle motion in this event is consistent with a simple *S* waveform but a large δt. Several results in the δt = 4–5 s range at shorter offsets were significantly reduced, suggesting that these may have originally had a problem with *P* wave contamination. Many of the other results were improved, mostly by the recovery of shear wave energy from the vertical component. The measured (back azimuth corrected) fast directions average 84.2 ± 23° for the new results compared to 111.0 ± 31° for the old (errors are 1 SD). Figure 12 shows a polar histogram of the new polarization results. We still interpret this as a general trend of *SH* leading *SV*, which suggests a roughly vertically oriented transversely isotropic medium (Figure 13). This would be consistent with the lack of *SKS/SKKS* phase splitting observed at the Australian stations.

[17] Figure 10e shows the variation of shear wave splitting as a function of event latitude. This shows that the minimum shear wave splitting occurs at around 23°S latitude. This was noted in WKB and is even clearer in the new results. This maybe significant; the transition between the Tonga and Kermadec subducting slabs is at around 25°S [e.g., *Hamburger and Isacks*, 1987]. This suggests that the effect might be linked to the subduction process, even though, as shown by WKB, anisotropy in the slab itself is unlikely as a complete explanation of these results.

4.2. Modeling

[18] Figure 10 also shows several possible models of mantle anisotropy. These are generated using ray tracing, and are parameterized with velocities from the IASP91 [*Kennett and Engdahl*, 1991] reference model, with one or more layers of anisotropy imposed. In order for the anisotropy to be invisible to *SKS*/*SKKS* phases we model the anisotropy as vertical transverse isotropy (VTI). This form of anisotropy (also called polar or radial anisotropy) has velocities which are invariant about a single vertical symmetry axis. This form of anisotropy is often parameterized with the Thomsen parameters [*Thomsen*, 1986] ϵ, γ, and δ. A horizontally traveling shear wave propagating in such a medium will be split into two: one parallel to

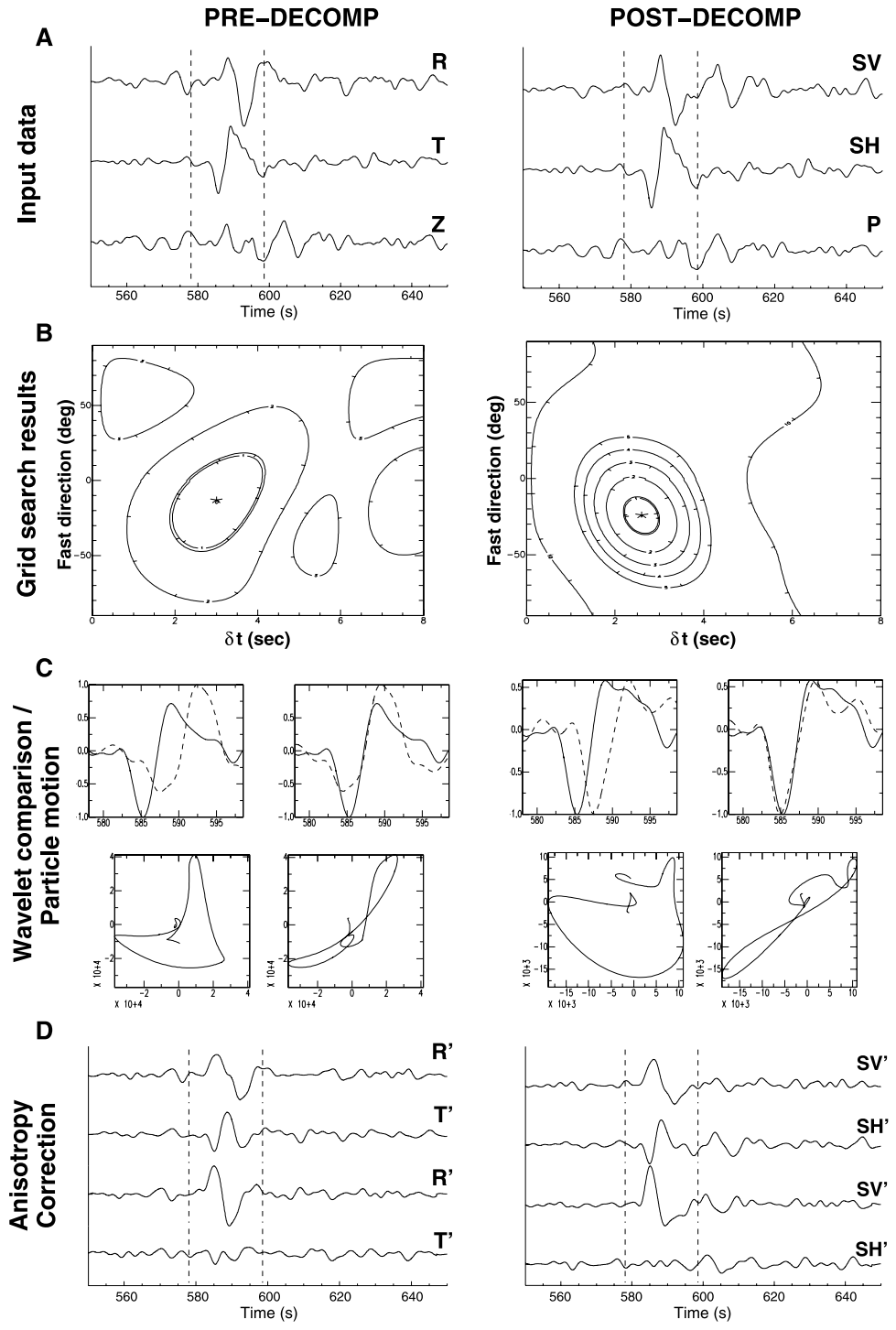

Figure 8. Comparison between results of shear wave splitting analysis before and after wave field decomposition for event 1997247 recorded at TAU. Figures 8a–8d are as described for Figures 4a–4d. It is clear that the postdecomposition result is superior. The transverse energy (Figure 8c) and the particle motion (Figure 8d) are more convincingly corrected, and the chosen solution is better constrained (Figure 8b). The improvement seems to be primarily due the recovery of *SV* wave energy from the vertical component (Figure 8a). The results prior to wave field decomposition are $\delta t = 3.0 \pm 0.55$ s and $\phi = -13 \pm 16°$, and afterward they are $\delta t = 2.6 \pm 0.20$ s and $\phi = -24 \pm 6°$.

the axis of symmetry (*SV*) and one perpendicular (*SH*). The sign of the Thomsen parameters determines which of these waves leads the other. The only case where no such splitting will be observed is where the incident shear wave is polarized perpendicular or parallel to the symmetry axis (see Figure 13). This would be the case for *SKS*/*SKKS* as the wave is polarized in the radial-vertical plane by the *P*-to-*S* conversion at the core-mantle bound-

Figure 9. Further examples of shear wave splitting results from the reprocessed Tonga-Australia data set. (top) Fast and slow (amplitude normalized) waveform before and after correction for the determined shear wave splitting parameters. (middle) Particle motion before and after correction. (bottom) Results of the grid search over δt and ϕ. The events shown are (a) 1988070 at CAN (Δ = 31.8); (b) 1996310 at WRAB (Δ = 42.4); (c) 1999099 at NWAO (Δ = 52.8); and (d) 1996336 at CTAO (Δ = 32.4).

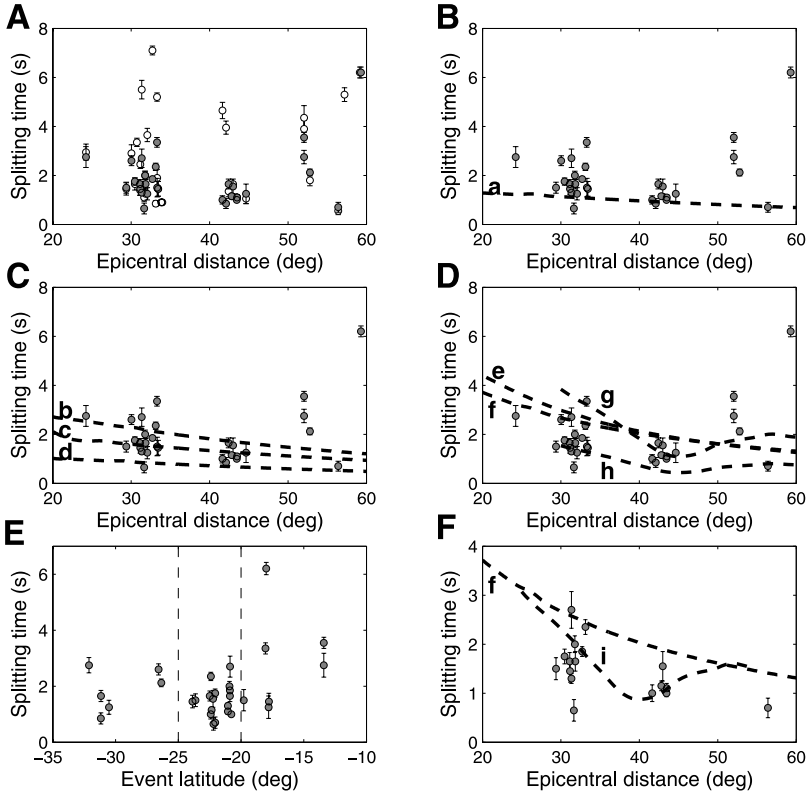

Figure 10. Shear wave splitting δt against epicentral distance and event latitude for the reprocessed Tonga-Australia data. Figure 10a shows the data from WKB (open circles) and the reprocessed data (solid circles) for comparison. Figures 10b–10d show the new data compared to the splitting predicted for models placing transverse isotropy in the upper (Figure 10b), transition zone (Figure 10c), and below 660 km (Figure 10d). Figure 10e shows δt against event latitude. The events with epicenter latitudes between 20°S and 25°S only are plotted in Figure 10f. The models included are model a, 4% VTI between 35 and 250 km [after *Gaherty and Jordan*, 1995]; model b, 4% VTI between 520 and 660 km (lower transition zone); model c, 4% VTI between 35 and 250 km and 2% VTI between 410 and 520 km; model d, 4% VTI between 410 and 520 km (upper transition zone); model e, 4% VTI between 660 and 770 km (uppermost lower mantle, preferred model of WKB); model f, 4% VTI between 35 and 250 km and 2% VTI between 660 and 770 km; model g, 10% TTI aligned by a lower mantle upwelling below subduction zone (see Figure 14); model h, 4% TTI aligned by a lower mantle upwelling below the subduction zone; model i, 8% TTI aligned by a lower mantle upwelling below the subduction zone.

ary. One example of where this symmetry of anisotropy is observed is a stack of thin (i.e., less than the dominant wavelength) layers with contrasting elastic properties [see, e.g., *Backus*, 1962].

[19] Two classes of model are tested. The first involves one-dimensional models of VTI layers at different depths. The second involves three-dimensional models where the axis of symmetry of the anisotropy is rotated from the vertical direction (tilted transverse isotropy TTI) according to some hypothetical flow pattern. Figure 14 shows an example of this. Here anisotropy below 660 km has been rotated to represent flow associated with an upwelling in the uppermost lower mantle, as postulated by *Gurnis et al.* [2000] to account for the high stresses observed in the Tonga subduction zone.

[20] It is clear that VTI confined to the upper mantle is an inadequate explanation for the magnitude of shear wave splitting we observe (model a). The models allowing anisotropy in the transition zone and uppermost lower mantle are much more effective at generating splitting, particularly those placing anisotropy below 520 km (models e–i). Of these models we prefer those which place anisotropy beneath 660 km, as perovskite in the lower mantle has a strong S wave anisotropy, whereas ringwoodite above 660 km is thought to be nearly isotropic [see, e.g., *Mainprice et al.*, 2000]. Models of this kind explain our results for most of the range of epicentral distances, though the very large splits at the furthest offsets are difficult to explain entirely by any of the models. Models which have a rotation of anisotropy in the uppermost lower mantle do show more complex behavior with epicentral distance (models g, h, and i in Figure 10), showing minimum splitting at around 45°, making them a possible candidate to explain the variation in the real data. If we look only at the data in the central region of the Tonga slab (between 20 and 25°S, Figure 10f), there is a more obvious reduction of splitting with distance. In this region the data still cannot be explained by upper mantle VTI, but here a midmantle VTI model adequately predicts the splitting magnitude in

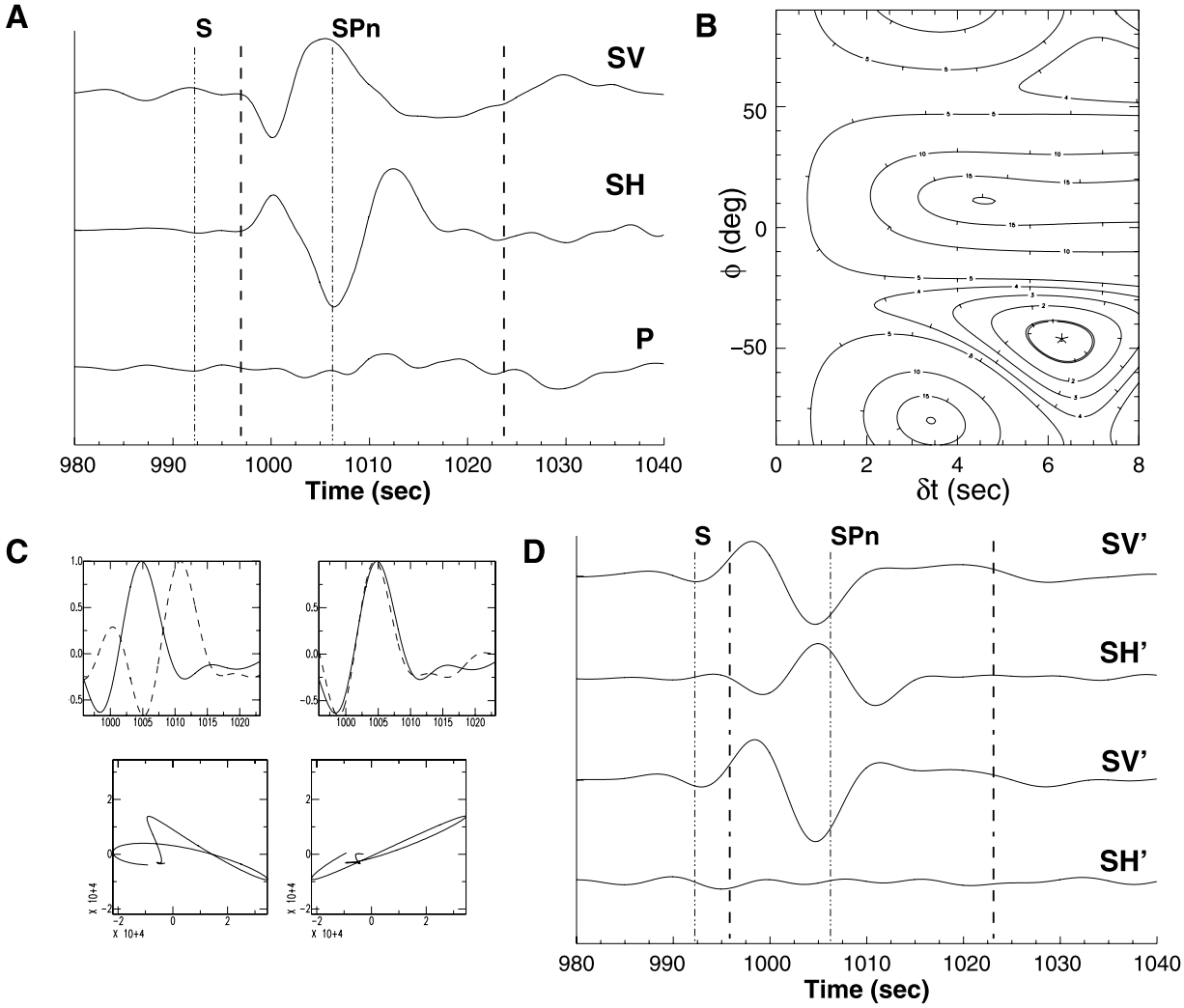

Figure 11. Shear wave splitting analysis of event 1994068 at NWAO. Figures 11a–11d are as described for Figure 4, and the analysis window is shown by the vertical dashed lines. This analysis shows a well constrained splitting result with rather convincing minimization of transverse energy (Figure 11d) and particle motion (Figure 11c). The best fitting shear wave splitting parameters were determined to be δt = 6.3 ± 0.35 s and $\phi = -46 \pm 4°$. To remove noise, the seismograms were filtered using a band-pass filter with corner frequencies of 0.02 and 0.15 Hz. The chosen filter affects the measurement only slightly, and the determined δt and ϕ always fall within the error bars of the mean result.

the data across the range of epicentral distances. Several of the larger δt measurements at large epicentral distance come from the northern part of the subduction zone, where the slab is highly contorted, a factor which may influence the anisotropy. All of the models tested, including those with a rotated axis of symmetry, predict a horizontal fast shear wave, as is observed in the data.

5. Discussion

[21] A previous study of the Tonga region using *SKS*/*SKKS* waves has suggested an isotropic midmantle region [*Fischer and Wiens*, 1996]; however, a VTI style of anisotropy would generate no splitting in these phases. This study has been extended by *Smith et al.* [2001] to include ocean bottom sensors in the Lau back arc and Tonga forearc. The pattern of splitting observed is more complex than that observed by *Fischer and Wiens* [1996], and this is interpreted as a complicated pattern of asthenospheric flow because of the influence of the Samoan plume. This events used in this study are local events beneath the Lau back arc. Most of these are of intermediate depth (150–300 km) and hence are probably not sensitive to the region of anisotropy which affects our data. Similarly, the deep events we use do not sample the region where this complex mantle flow is postulated to occur.

[22] Recent work by *Chen and Brudzinski* [2003] looks for delays between the *SH* and *SV* phases recorded at stations PVC and NOUC (island stations located around 20° east of the Tonga subduction zone). The *S* phase at this distance is triplicated, and they use modeling to interpret splitting for the different branches. They observe up to 3 s of splitting in phases from the northern Tonga trench (north of 23°S) and null splitting in the events from the southern part of the trench. They interpret this

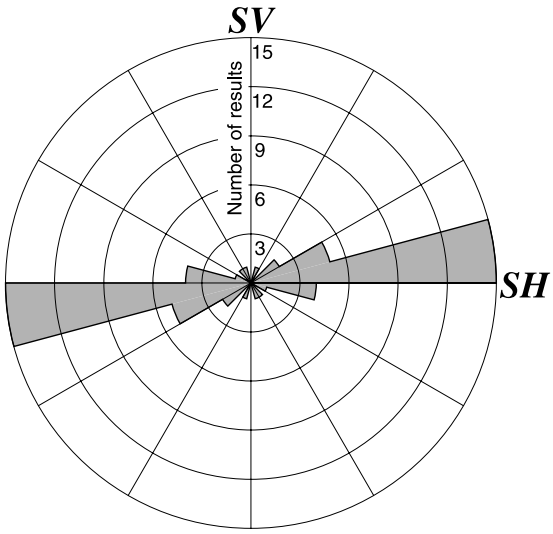

Figure 12. Polar histogram of polarization of the fast shear wave for the reprocessed Tonga-Australia results. The average polarization is 82.9 ± 9.8°, showing a general trend of *SH* leading *SV*.

as being associated with a detached slab remnant lying above the main subducting slab, the existence of which is inferred from outboard earthquakes [*Chen and Brudzinski*, 2001]. This explanation for the anisotropy does not seem to adequately explain our results. First, we have observed significant splitting in *S* phases from events at latitudes south of 23°S. Second, the longer epicentral distances for our data means that even north of 23°S the *S* phase leaves the anomalous region very quickly, without sufficient time to accrue the observed splitting given VTI with a strength of 0.9 ± 0.3%, as inferred by *Chen and Brudzinski* [2003].

[23] It should be noted, however, that the two studies are sensitive to different regions. *Chen and Brudzinski* [2003] use short epicentral-distance transition zone and upper mantle ray paths, while our study uses longer ray paths with a much larger proportion in the lower mantle. Thus these phases spend a negligible time in the region where *Chen and Brudzinski* [2003] infer anisotropy to lie. It is therefore entirely possible that significant anisotropy is present in both regions.

[24] Models which place TI-like anisotropy in the uppermost lower mantle are the most effective at generating splitting, due to the more horizontal ray paths through the region, and explain the data at most of the range of epicentral distances. Scenarios for these models have been discussed in WKB and are further outlined in Figure 15.

[25] Anisotropy at this depth can be explained by either lattice-preferred orientation (LPO) of anisotropic crystals or shape-preferred orientation (SPO) of included materials. Several candidate scenarios (Figures 15a, 15b, and 15c) involve the LPO alignment of lower mantle perovskite, in a global or large regional boundary layer or by local dynamic features. $MgSiO_3$ perovskite is highly anisotropic in a single-crystal form [see, e.g., *Mainprice et al.*, 2000]. Furthermore, recent experimental measurements by *Cordier et al.* [2004] using $MgSiO_3$ perovskite at uppermost lower mantle temperature and pressure conditions show that the deformation is dominated by dislocation creep. This mechanism is required for the LPO formation of a polycrystalline anisotropic fabric. Numerical modeling also suggests that this mechanism may dominate in the high-stress regimes near subducting slabs [*McNamara et al.*, 2001]. The cause of deformation in the uppermost lower mantle could have several explanations. The most obvious perhaps is the subducting slab itself. Numerical modeling has demonstrated large, long-range stresses associated with the impingement of the subducting slab on the 660 km discontinuity [*Kusznir*, 2000; *Nippress et al.*, 2003]. *Gurnis et al.* [2000] postulate the presence of an upwelling in the lower mantle below

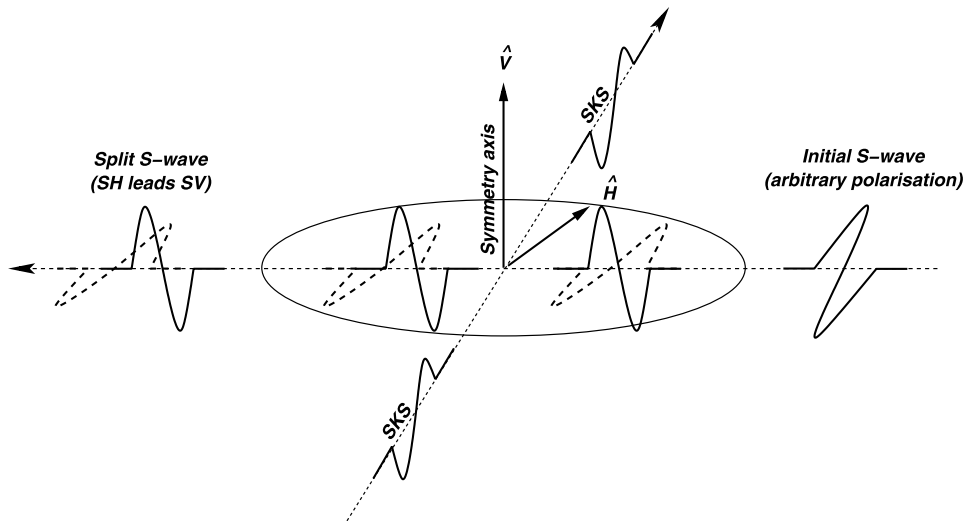

Figure 13. Effect of VTI (transverse anisotropy with a vertical axis of symmetry) style anisotropy on a horizontally propagating *S* wave and an *SKS* phase. The *S* phase is split into two shear waves *SV* and *SH*. In this case the *SH* (dashed line) leads *SV* (solid line). The *SKS* phase is already polarized into the radial-vertical plane and therefore is not split by the VTI medium.

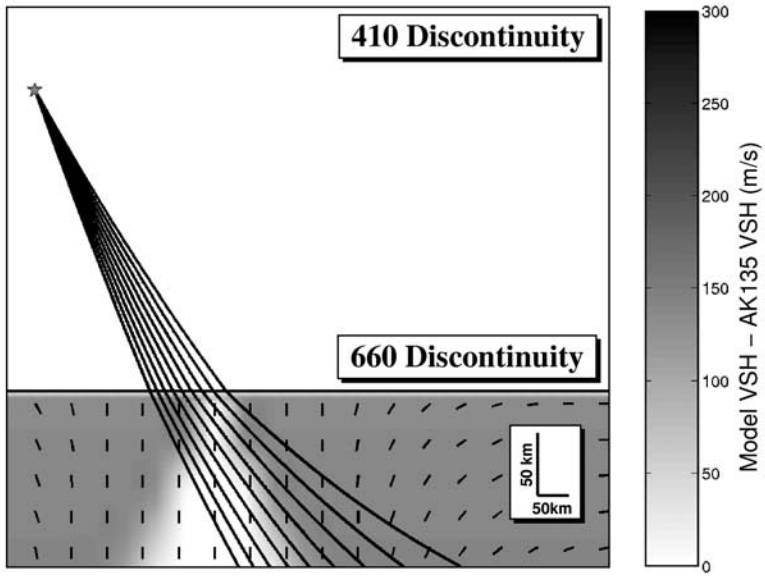

Figure 14. Example model of midmantle anisotropy due to an upwelling in the uppermost lower mantle beneath the descending Tonga slab [*Gurnis et al.*, 2000]. The shading scale denotes the difference between the (horizontal) shear wave velocity in the model and AK135, and the black vectors denote the symmetry axis of the imposed transverse isotropic media. The black lines are example ray paths.

the Tonga-Kermadec subduction zone to explain the observations of high stresses in the slab. The collision of two such features could generate horizontal flow in the region of interest.

[26] The final scenario postulates the SPO alignment of inclusions of subducted material in a "megalith" beneath 660 km [*Ringwood*, 1994]. Aligned inclusions of material with contrasting elastic properties to those of the matrix can be extremely efficient at causing anisotropy, even for very small volume fractions [*Kendall and Silver*, 1998]. One possible candidate for this material is basaltic melt, which has been suggested to be near its solidus at the top of the lower mantle [*Hirose et al.*, 1999].

[27] The geographical variation of splitting magnitude may also provide insight into the cause of the anisotropy; we see the lowest amounts of shear wave splitting in earthquakes around 23°S. This is the latitude of the transition between the Tonga and Kermadec subduction zones which may suggest a link to, or at least a contribution from, the subduction process.

6. Conclusions

[28] *Wookey et al.* [2002] study shear wave splitting in *S* phases from deep earthquakes in the Tonga-Kermadec subduction zone recorded at Australian seismic stations. In this study we have revisited the data set of WKB to assess the impact of shear-coupled *P* waves on the original results and the conclusions drawn from them. We have used reflectivity synthetics to show the potential problems caused by these phases and introduced wave field decomposition as a mechanism to remove them. Tests show that this technique is effective at minimizing these phases. We have reprocessed the data set of WKB after applying the wave

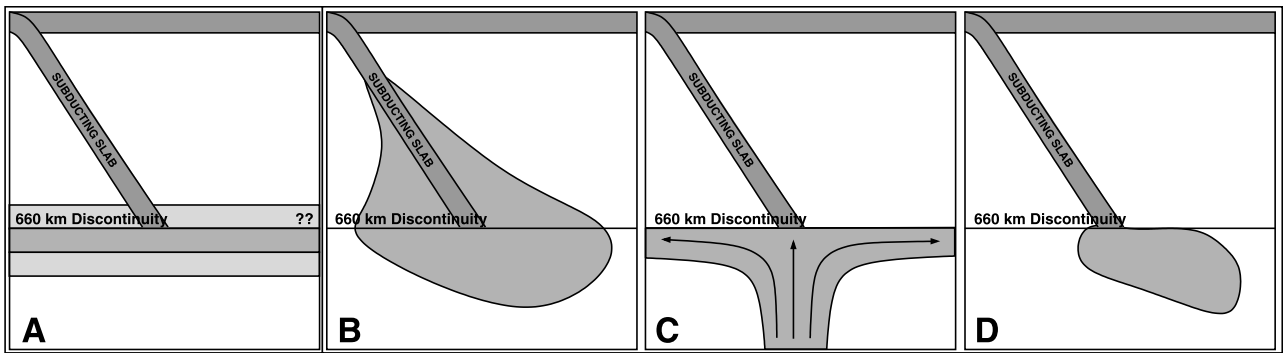

Figure 15. Possible scenarios of midmantle anisotropy. Three postulate the lattice-preferred orientation (LPO) of midmantle minerals (a) in a global boundary layer, (b) by stress fields associated with subduction [after, e.g., *Nippress et al.*, 2003], or (c) by an upwelling in the lower mantle [after *Gurnis et al.*, 2000]. (d) The final scenario is the shape-preferred orientation (SPO) of subducted material (for example, basaltic melt) in a "megalith" in the uppermost lower mantle [after, e.g., *Ringwood*, 1994].

field decomposition to the data. While some of our larger results at short distances are significantly reduced, many large results remain. The wave field decomposition also, in general, reduces the error in the results. We have modeled a number of scenarios postulated as a cause of anisotropy at these stations. These models show clearly that VTI anisotropy in the upper mantle beneath the stations is an inadequate explanation of our results. Thus we conclude that the source of the anisotropy is in the midmantle region near the source. Several scenarios are suggested to explain these results. These infer the presence of a significant region of deformation in the uppermost lower mantle, causing either the LPO alignment of $MgSiO_3$ perovskite or the SPO alignment of subducted material. This deformation may be linked to dynamic processes in the region. The results that we have presented show strong evidence of anisotropy in the midmantle region around the Tonga-Kermadec subduction zones. The precise location and cause of this anisotropy are still not well constrained, but this study provides insights into dynamic processes at work in the region which are not yet well understood.

[29] **Acknowledgment.** The authors would like to thank George Zandt, Renate Hartog, Joachim Saul, an anonymous reviewer, and the Associate Editor for useful comments and discussion.

References

Babůska, V., J.-P. Montanger, J. Plomerová, and N. Girardin (1998), Age dependent large-scale fabric of the mantle lithosphere as derived from surface-wave velocity anisotropy, *Pure Appl. Geophys.*, *151*, 257–280.

Backus, G. E. (1962), Long-wave elastic anisotropy produced by horizontal layering, *J. Geophys. Res.*, *67*, 4427–4440.

Barruol, G., and R. Hoffmann (1999), Upper mantle anisotropy beneath the Geoscope stations, *J. Geophys. Res.*, *104*, 10,757–10,773.

Bevis, M., et al. (1995), Geodetic observations of very rapid convergence and back-arc extension at the Tonga Arc, *Nature*, *374*, 249–251.

Blackman, D. K., J. A. Orcutt, D. W. Forsyth, and J.-M. Kendall (1993), Seismic anisotropy in the mantle beneath an oceanic spreading centre, *Nature*, *366*, 675–677.

Booth, D. C., and S. Crampin (1985), Shear-wave polarizations on a curved wavefront at an isotropic free surface, *Geophys. J. R. Astron. Soc.*, *83*, 31–45.

Bostock, M. G. (1998), Mantle stratigraphy and evolution of the Slave province, *J. Geophys. Res.*, *103*, 21,183–21,200.

Braun, M. G., G. Hirth, and E. M. Parmentier (2000), The effects of deep damp melting on mantle flow and melt generation beneath mid-ocean ridges, *Earth Planet. Sci. Lett.*, *176*, 339–356.

Brisbourne, A., G. Stuart, and J.-M. Kendall (1999), Anisotropic structure of the Hikurangi subduction zone, New Zealand; integrated interpretation of surface-wave and body-wave observations, *Geophys. J. Int.*, *137*, 214–230.

Chen, W.-P., and M. R. Brudzinski (2001), Evidence for a large-scale remnant of subducted lithosphere beneath Fiji, *Science*, *292*(5526), 2475–2479.

Chen, W.-P., and M. R. Brudzinski (2003), Seismic anisotropy in the mantle transition zone beneath Fiji-Tonga, *Geophys. Res. Lett.*, *30*(13), 1682, doi:10.1029/2002GL016330.

Clitheroe, G., and R. D. van der Hilst (1998), Complex anisotropy in the Australian lithosphere from shear-wave splitting in broad-band *SKS* records, in *Structure and Evolution of the Australian Continent*, *Geodyn. Ser.*, vol. 26, edited by J. Braun et al., pp. 73–78, AGU, Washington, D. C.

Clitheroe, G., O. Gudmundsson, and B. L. N. Kennett (2000), The crustal thickness of Australia, *J. Geophys. Res.*, *105*, 13,697–13,713.

Cordier, P., T. Ungár, L. Zsoldos, and G. Tichy (2004), Dislocation creep in $MgSiO_3$, *Nature*, *428*, 837–840.

Fischer, K. M., and D. A. Wiens (1996), The depth distribution of mantle anisotropy beneath the Tonga subduction zone, *Earth Planet. Sci. Lett.*, *142*, 253–260.

Fischer, K. M., M. J. Fouch, D. A. Wiens, and M. S. Boettcher (1998), Anisotropy and flow in Pacific suduction zone back-arcs, *Pure Appl. Geophys.*, *151*, 463–475.

Fouch, M. J., and K. M. Fischer (1996), Mantle anisotropy beneath northwest Pacific subduction zones, *J. Geophys. Res.*, *101*, 15,987–16,002.

Gaherty, J. B., and T. H. Jordan (1995), Lehmann discontinuity as the base of an anisotropic layer beneath continents, *Science*, *268*, 1468–1471.

Gripp, A. E., and R. G. Gordon (1990), Current plate velocities relative to the hotspots incorporating the NUVEL-1 global plate motion model, *Geophys. Res. Lett.*, *17*, 1109–1112.

Gudmundsson, O., and M. Sambridge (1998), A regionalised upper mantle (RUM) seismic model, *J. Geophys. Res.*, *103*, 7121–7136.

Gurnis, M., J. Ritsema, and H. J. Van Heist (2000), Tonga slab deformation: The influence of a lower mantle upwelling on a slab in a young subduction zone, *Geophys. Res. Lett.*, *27*, 2373–2376.

Hall, R., and W. Spakman (2002), Subducted slabs beneath the eastern Indonesia-Tonga region: Insights from tomography, *Earth Planet. Sci. Lett.*, *201*, 321–336.

Hamburger, M. W., and B. L. Isacks (1987), Deep earthquakes in the southwest Pacific: A tectonic interpretation, *J. Geophys. Res.*, *92*, 13,841–13,854.

Hirose, K., Y. Fei, Y. Ma, and H.-K. Mao (1999), The fate of subducted basaltic crust in the Earth's lower mantle, *Nature*, *397*, 53–56.

Kaneshima, S., and P. G. Silver (1992), A search for source-side mantle anisotropy, *Geophys. Res. Lett.*, *19*, 1049–1052.

Karato, S. (1998), Some remarks on the origin of seismic anisotropy in the D'' layer, *Earth Planets Space*, *50*, 1019–1028.

Kendall, J.-M. (1994), Teleseismic arrivals at a mid-ocean ridge; effects of mantle melt and anisotropy, *Geophys. Res. Lett.*, *21*, 301–304.

Kendall, J.-M. (2000), Seismic anisotropy in the boundary layers of the mantle, in *Earth's Deep Interior: Mineral Physics and Tomography From the Atomic to the Global Scale*, *Geophys. Monogr. Ser.*, vol. 117, edited by S. Karato et al., pp. 133–159, AGU, Washington, D. C.

Kendall, J.-M., and P. G. Silver (1998), Investigating causes of D″ anisotropy, in *The Core-Mantle Boundary Region*, *Geodyn. Ser.*, vol. 28, edited by M. Gurnis et al., pp. 97–118, AGU, Washington, D. C.

Kennett, B. L. N. (1991), The removal of free surface interactions from three-component seismograms, *Geophys. J. Int.*, *104*, 153–163.

Kennett, B. L. N., and E. R. Engdahl (1991), Traveltimes for global earthquake location and phase identifications, *Geophys. J. Int.*, *105*, 429–465.

Kennett, B. L. N., E. R. Engdahl, and R. Buland (1995), Constraints on seismic velocities in the Earth from traveltimes, *Geophys. J. Int.*, *122*(1), 108–124.

Kusznir, N. J. (2000), Subduction body force stresses and viscosity structure at the 410 km and 660 km phase transitions, *Eos Trans. AGU*, *81*(48), Fall Meet. Suppl., Abstract T51E-10.

Lay, T., Q. Williams, E. J. Garnero, L. Kellogg, and M. E. Wysession (1998), Seismic wave anisotropy in the D″ region and its implications, in *The Core-Mantle Boundary Region*, *Geodyn. Ser.*, vol. 28, edited by M. Gurnis et al., pp. 299–318, AGU, Washington, D. C.

Mainprice, D., G. Barruol, and W. B. Ismaïl (2000), The seismic anisotropy of the Earth's mantle: From single crystal to polycrystal, in *Earth's Deep Interior: Mineral physics and Tomography From the Atomic to the Global Scale*, *Geophys. Monogr. Ser.*, vol. 117, edited by S. Karato et al., pp. 237–264, AGU, Washington, D. C.

McNamara, A. K., S. Karato, and P. E. Van Keken (2001), Localization of dislocation creep in the lower mantle: Implications for the origin of seismic anisotropy, *Earth Planet. Sci. Lett.*, *191*, 85–99.

Montagner, J.-P. (1998), Where can seismic anisotropy be detected in the Earth's mantle? In boundary layers . . ., *Pure Appl. Geophys.*, *151*, 223–256.

Montagner, J.-P., and B. L. N. Kennett (1996), How to reconcile body-wave and normal-mode reference Earth models, *Geophys. J. Int.*, *125*, 229–248.

Mueller, G. (1985), The reflectivity method: A tutorial, *J. Geophys.*, *58* (1–3), 153–174.

Nippress, S. E., N. Kusznir, and J.-M. Kendall (2003), Mantle seismic anisotropy beneath the 660 km phase transition generated by subduction body force stresses, *Geophys. Res. Abstr.*, *5*, Abstract 03476.

Özalaybey, S., and W. P. Chen (1999), Frequency-dependent analysis of *SKS/SKKS* waveforms observed in Australia: Evidence for null birefringence, *Phys. Earth Planet. Inter.*, *114*, 197–210.

Ringwood, A. E. (1994), Role of the transition zone and 660 km discontinuity in mantle dynamics, *Phys. Earth Planet. Inter.*, *86*, 5–24.

Russo, R. M., and P. G. Silver (1994), Trench-parallel flow beneath the Nazca plate from seismic anisotropy, *Science*, *263*, 1105–1111.

Saul, J., and L. Vinnik (2003), Mantle deformation or processing artefact?, *Nature*, *422*, 136.

Savage, M. K. (1999), Seismic anisotropy and mantle deformation: What have we learned from shear wave splitting?, *Rev. Geophys.*, *37*, 65–106.

Silver, P. G. (1996), Seismic anisotropy beneath the continents: Probing the depths of geology, *Annu. Rev. Earth Planet. Sci.*, *24*, 385–432.

Silver, P. G., and W. W. J. Chan (1991), Shear-wave splitting and subcontinental mantle deformation, *J. Geophys. Res.*, *96*, 16,429–16,454.
Smith, G. P., D. A. Wiens, K. M. Fischer, L. M. Dorman, S. C. Webb, and J. A. Hildebrand (2001), A complex pattern of mantle flow in the Lau Backarc, *Science*, *292*, 713–716.
Smith, W., and D. Sandwell (1997), Global seafloor topography from satellite altimetry and ship depth soundings, *Science*, *227*, 195–196.
Thomas, C., and J.-M. Kendall (2002), The lowermost mantle beneath northern Asia—II. Evidence for lower-mantle anisotropy, *Geophys. J. Int.*, *151*, 296–308.
Thomsen, L. (1986), Weak elastic anisotropy, *Geophysics*, *51*, 1954–1966.
Tong, C., O. Gudmundsson, and B. L. N. Kennett (1994), Shear-wave splitting in refracted waves returned from the upper-mantle transition zone beneath northern Australia, *J. Geophys. Res.*, *99*, 15,783–15,797.
Trampert, J., and H. J. Van Heijst (2002), Global azimuthal anisotropy in the transition zone, *Science*, *296*, 1297–1299.
Widiyantoro, S., B. L. N. Kennett, and R. D. van der Hilst (1999), Seismic tomography with *P* and *S* data reveals lateral variations in the rigidity of deep slabs, *Earth Planet. Sci. Lett.*, *173*, 91–100.
Wolfe, C. J., and S. C. Solomon (1998), Shear-wave splitting and implications for mantle flow beneath the MELT region of the East Pacific Rise, *Science*, *280*, 1230–1232.
Wookey, J., J.-M. Kendall, and G. Barruol (2002), Mid-mantle deformation inferred from seismic anisotropy, *Nature*, *415*, 777–780.
Wookey, J., J.-M. Kendall, and G. Barruol (2003), Reply to Mantle deformation or processing artefact?, *Nature*, *422*, 136.
Zandt, G., and G. E. Randall (1985), Observations of shear-coupled *P*-waves, *Geophys. Res. Lett.*, *12*(9), 565–568.

J.-M. Kendall and J. Wookey, School of Earth Sciences, University of Leeds, Woodhouse Lane, Leeds LS2 9JT, UK. (m.kendall@earth.leeds.ac.uk; jwookey@earth.leeds.ac.uk)